Defects in magnesium and its alloys by atomistic simulation: Assessment of semi-empirical potentials

Hexin Wang, Julien Guénolé, Sandra Korte-Kerzel, Talal Al-Samman, Zhuocheng Xie

Computational Materials Science 240 (2024) 113025

Contents lists available at ScienceDirect

Computational Materials Science

journal homepage: www.elsevier.com/locate/commatsci

Full Length Article

Defects in magnesium and its alloys by atomistic simulation: Assessment of semi-empirical potentials

Hexin Wang [a,*], Julien Guénolé [b], Sandra Korte-Kerzel [a], Talal Al-Samman [a], Zhuocheng Xie [a,*]

[a] Institute of Physical Metallurgy and Materials Physics, RWTH Aachen University, 52056 Aachen, Germany
[b] CNRS, Université de Lorraine, Arts et Métiers ParisTech, LEM3, 57070 Metz, France

ARTICLE INFO

Keywords:
Atomistic simulation
Magnesium
Semi-empirical potentials
Dislocations
Grain boundary
Solute segregation

ABSTRACT

Dislocation and grain boundary properties of Mg and its alloys were assessed by atomistic simulations using various semi-empirical potentials. The results were compared with available experimental data and first-principles calculations. It was observed that embedded-atom method (EAM) potentials notably deviated from experimental observations in dislocation properties, especially for pyramidal dislocations. For the coincident site lattice (CSL) $\Sigma 7$ grain boundary, the choice of interatomic potential significantly influences the minimum energy structures, namely, the T-type structure is stable when using modified embedded-atom method (MEAM) potentials, whereas the A-type structure demonstrates stability when EAM potentials are applied. Furthermore, a strong correlation between the per-site segregation energies of alloying elements and the excess free volumes at grain boundaries was identified across all tested potentials. The outcomes of this work pave the way for potential selection in future large-scale modeling of small-scale plasticity in Mg and its alloys.

1. Introduction

Magnesium, as one of the lightest metallic materials, plays an important role in industrial manufacturing due to its superior properties, such as excellent dimensional stability, high specific strength, relative abundance and good recyclability [1]. However, extensive industrial application of magnesium alloys still faces considerable constraints due to their limited formability and ductility at room temperature. This is mainly due to the hexagonal close-packed (hcp) crystal structure of Mg, which leads to high plastic anisotropy and restricts the number of easily activated slip systems [2]. To address this limitation and meet industrial demands, a comprehensive scientific understanding of plastic deformation mechanisms in Mg and the complex interaction between solutes, dislocations and interfaces is crucial.

Atomistic simulations using high-performance computing have gained significant popularity as a powerful scientific approach for investigating computationally intensive problems of the atomistic behaviors in materials. Particularly in the field of lattice defects, atomistic simulations have been successfully applied to predict generalized stacking fault energies (GSFE) [3–5], dislocation motion [6–8], grain boundary (GB) motion [9–11] and segregation [12–14]. Compared with first-principles methods, such as density-functional theory (DFT), atomistic simulations are less constrained by the simulation time and length scales. This advantage allows atomistic simulations to provide valuable insights into large-scale phenomena, including defect-defect interactions, which are not accessible by first-principles methods.

As classical semi-empirical potentials, embedded atom method (EAM) [15] and modified embedded atom method (MEAM) [16] potentials are commonly employed in the atomistic simulations of Mg. The EAM potential was developed to improve the pair potential approach by including the effect of the local electron density. The total energy in EAM is formulated as:

$$E_{\text{total}} = \sum_i F(\rho_i) + \frac{1}{2}\sum_i \sum_j \phi(r_{ij}) \tag{1}$$

where $\phi(r_{ij})$ is the pair potential function depending on the distance (r_{ij}). $F(\rho_i)$ is the embedding function for atom i, dependent on the local electron density ρ_i at its site. ρ_i is determined by:

$$\rho_i = \sum_{j \neq i} f(r_{ij}) \tag{2}$$

where $f(r_{ij})$ is the electron density due to the jth particle [15]. One of the widely used EAM potentials for Mg is the one developed by Liu and Adams [17]. Originally designed for the Al–Mg system to study the segregation of solute Mg to grain boundaries in Al, this potential has become popular for studying deformation mechanisms in Mg alloys [18–22]. Another frequently used EAM potential for Mg was developed by Sun et al. [23] to simulate interfacial free energies

* Corresponding authors.
E-mail addresses: wang@imm.rwth-aachen.de (H. Wang), xie@imm.rwth-aachen.de (Z. Xie).

https://doi.org/10.1016/j.commatsci.2024.113025
Received 4 December 2023; Received in revised form 8 April 2024; Accepted 8 April 2024
Available online 16 April 2024

during solidification in hcp metals. This potential has also been widely utilized for various investigations, including dislocations [22,24–26] and fracture mechanisms [27,28]. MEAM potentials, in comparison to EAM potentials, incorporate angular dependence in the electron density, thus providing more sophisticated interatomic interactions. The total energy in MEAM follows Eq. (1), where the EAM electron density ρ_i is replaced with $\bar{\rho}$, calculated as:

$$\bar{\rho} = \rho_i G(\Gamma) \tag{3}$$

where $G(\Gamma)$ accounts for the angular dependence in the electron density [16]. MEAM potentials are therefore more computationally expensive, i.e. they often require an order of magnitude more computational resources than EAM potentials. Representative MEAM potentials for Mg are the ones developed by Kim et al. [29] and its modified version by Wu et al. [30]. Both Kim and Wu et al.'s potentials are widely applied to various Mg-related atomic-scale investigations [31–35]. Fan et al. [31] applied the potential by Kim et al. to study the temperature effects on the dislocation mobility on pyramidal slip planes in Mg. Sato et al. [36] chose the potential by Wu et al. to investigate the thermally activated migration of $\{1\,0\,\bar{1}\,2\}$ twin interfaces. However, irrespective of the potential type, it remains challenging to encompass all the features within one single potential to accurately predict the physical behaviors of the material. This underscores the significance of careful potential selection, as the accuracy of atomistic simulations relies heavily on the choice of suitable potential. For instance, it has been reported that the application of EAM potentials, such as the ones from Liu or Sun can lead to unrealistic GSFE values and Peierls barriers [30]. Therefore, to optimize the selection of potentials and ensure the physical representation of material properties in simulations, a systematic assessment of the relevant interatomic potentials for different Mg-X systems is essential.

In this work, we first calculated basic bulk properties including lattice constants, cohesive energies, elastic tensors and moduli, as well as stacking fault energies (SFEs) and twin boundary energies (TBEs). The generalized stacking fault energies (GSFEs) of the basal $\{0\,0\,0\,1\}$, prismatic $\{1\,0\,\bar{1}\,1\}$, pyramidal I $\{1\,0\,\bar{1}\,1\}$ and pyramidal II $\{1\,1\,\bar{2}\,2\}$ planes were calculated and compared with previous DFT results. In addition, the core structures, splitting distances and Peierls stresses of both the pure edge and screw dislocations on these four slip planes were investigated. Furthermore, we compared the performance of these potentials by evaluating the GB energies of the $\{1\,0\,\bar{1}\,1\}$ compression twin (CT) and the $\{1\,0\,\bar{1}\,2\}$ tensile twin (TT), as well as one of the most studied GBs in hcp metals, the $\Sigma7$ $\{1\,2\,\bar{3}\,0\}$ $\langle 0\,0\,0\,1\rangle$ 21.8° symmetric boundary. In addition to the $\Sigma7$ GB, we calculated the energies of several CSL $\langle 0\,0\,0\,1\rangle$ symmetric tilt GBs, which help gain insight into their structures and properties. Finally, to investigate the segregation behavior of popular alloying elements in Mg, we calculated the per-site segregation energies of the three aforementioned CT, TT and $\Sigma7$ GBs.

2. Simulation methods

The atomistic simulations presented in this study were conducted using the open-source code Large-scale Atomic/Molecular Massively Parallel Simulator (LAMMPS) [37]. Molecular statics methods were applied for the simulations, wherein all calculations were carried out at 0 K. To achieve minimum energy configurations, both the conjugate gradient and fast inertial relaxation engine (FIRE) algorithms [38,39] were employed, with the force tolerance of 10^{-8} eV/Å.

In this work, we studied the performance of many potentials and for brevity will refer to them in the following using the lead author's name and the type of potential, i.e. EAM or MEAM. We benchmarked five popularly employed EAM potentials including Liu_EAM [17], Wilson_EAM [40], Mendelev_EAM [41], Pei_EAM [42] and Sheng_EAM [43] potentials. As for the MEAM potentials, we tested three potentials including Kim_MEAM [29], Ahmad_MEAM [44] and Dickel_MEAM [45] potentials. It should be pointed out that we selected several Mg binary MEAM potentials, including Mg–Al [46], Mg–Ca [29], Mg–Li [47], Mg–Nd [48], Mg–Pb [48], Mg–Sn [29], Mg–Y [29], and Mg–Zn [49], using the same parameters to describe the Mg–Mg pair interaction as in the Kim_MEAM [29]. For a more intuitive comparison, all these potentials are referred to as Kim_MEAM potential. Note that the Ahmad_MEAM Mg–Y potential is based on the Mg–Mg MEAM potential of Wu [30], and the Mendelev_EAM Mg–Al potential is based on the Mg EAM potential of Sun [23].

The construction of the atomic samples was facilitated using Atomsk [50]. In the benchmark of basic bulk properties, samples were constructed with approximate dimensions of 4 nm × 5 nm × 5 nm, comprising a total of 4,800 Mg atoms. Periodic boundary conditions (PBC) were employed in all three directions for the calculations. When computing the SFEs, non-periodic boundary conditions (nPBC) were applied along the normal direction of the stacking fault plane, while the other two directions were maintained periodic. In the calculation of GSFE, PBC were implemented in the x and y directions, and the sample dimensions in these two directions were approximately twice the cutoff length of the potential. Meanwhile, nPBC were applied along the z direction with a dimension 5 times larger than in the x and y directions. The upper half of the sample was incrementally and rigidly shifted along the slip direction in the xy plane. Energy minimization was performed after each incremental movement with all atoms fixed in the x and y directions and only allowed to relax in the z direction. The GSFE was calculated based on the following Eq. (4):

$$\gamma_{\mathrm{GSF}} = \frac{E_{\mathrm{f}} - E_0}{l_{\mathrm{x}} \times l_{\mathrm{y}}} \tag{4}$$

where E_0 and E_{f} denote the total energies of the crystal before and after rigid shifting. l_{x} and l_{y} are the simulation box dimensions .

To construct edge and screw dislocations on the basal, prismatic, pyramidal I & II planes, we followed the method detailed in [51]. All the samples were constructed with the dislocation line parallel to the y axis, and the z axis perpendicular to the slip plane. PBC were applied in the dislocation line direction (y) and slip direction (x), while nPBC were used along the z axis. The dimensions of samples in the x and z directions were approximately 30 nm, while the dimension along the y direction was larger than twice the cutoff of the potentials, which was about 1.5 nm. However, it should be noted that the samples containing the pyramidal I edge dislocation had a long periodic unit in the dislocation line direction of approximately 9 nm. After the relaxation, the dislocation structures were analyzed using the common neighbor analysis (CNA) method [52] implemented in OVITO [53] to determine the dislocation splitting distances and visualized using the Nye tensor [54] and differential displacement maps [55] with the cutoff and angle thresholds for hcp crystals defined in [56]. The quasi-static method was applied to calculate the Peierls stress [57]. To induce the desired simple shear stress, the sample was shear deformed and force boundary conditions were applied to the atoms at the outermost layers of both the upper and lower z surfaces. The shear deformation and applied forces increased incrementally. After each step, an energy minimization process was conducted to relax the system and achieve a stable configuration under the applied shear stress. The Peierls stress was determined as the applied shear stress at which the dislocation moves more than a Burgers vector.

To construct the $\langle 0\,0\,0\,1\rangle$ symmetric tilt GBs, a Mg unit cell with the orientation x-$[1\,1\,\bar{2}\,0]$, y-$[1\,\bar{1}\,0\,0]$, and z-$[0\,0\,0\,1]$ was subjected to a rotation along the z-axis with half of the tilt angles ($\pm\frac{\theta}{2}$). Following the rotation, the periodicity of the supercell was restored in all directions to maintain PBC. Then, two symmetrically rotated crystals were merged together along the x-axis, which is set to have nPBC. Additionally, the distance between the GB plane and the semi-fixed surfaces was set to approximately 20 nm to eliminate their interaction. Microscopic degrees of freedom in the GB structures were explored through rigid-body translations in all directions and atom deletion within critical

Table 1
Calculated material properties of tested Mg potentials, in comparison with the experimental or DFT data. Values listed are lattice parameters a and c, cohesive energy, elastic constants including C_{11}, C_{12}, C_{13}, C_{33} and C_{44}, stacking fault energies of I_1 and I_2, $\{10\bar{1}1\}$ compression twin (CT) and $\{10\bar{1}2\}$ tensile twin (TT).

Potentials	Kim_MEAM	Ahmad_MEAM	Dickel_MEAM	Liu_EAM	Wilson_EAM	Mendelev_EAM	Pei_EAM	Sheng_EAM	Experiment/DFT
Lattice parameter, a (Å)	3.209	3.187	3.197	3.196	3.185	3.184	3.217	3.181	3.209 [59]
Lattice parameter, c (Å)	5.197	5.172	5.188	5.187	5.188	5.184	5.136	5.201	5.211 [59]
Cohesive energy (eV)	−1.55	−1.51	−1.51	−1.51	−1.53	−1.53	−1.51	−1.51	−1.51 [60]
C_{11} (GPa)	62.8	64.3	64.3	62.4	69.1	68.8	53.6	67.4	63.5 [61]
C_{12} (GPa)	26.0	25.5	25.3	26.3	26.7	26.1	24.4	32.6	25.9 [61]
C_{13} (GPa)	21.2	20.3	20.3	22.1	15.4	16.0	23.3	16.2	21.7 [61]
C_{33} (GPa)	69.6	70.9	71.0	67.8	69.0	69.5	78.6	65.7	66.5 [61]
C_{44} (GPa)	17.1	18.0	18.1	18.3	12.3	12.7	23.0	13.9	18.4 [61]
E_{SF}^{I1} (mJ/m^2)	15.1	11.3	11.5	27.1	22.5	22.1	16.9	−0.7	13.1 [62]
E_{SF}^{I2} (mJ/m^2)	30.0	22.5	23.0	54.2	45.0	44.1	32.5	−1.7	27.7 [62]
E_{CT} (mJ/m^2)	85.6	89.9	91.5	75.2	112.0	106.5	109.0	87.8	85.5 [62]
E_{TT} (mJ/m^2)	144.0	149.0	153.7	122.1	109.0	114.1	150.7	123.1	118.1 [62]

distances of 0 to 0.2 nm at the GBs [58]. After relaxation of the samples, the GB energy E_{GB} was calculated using Eq. (5):

$$E_{GB} = \frac{E(N) - N E_{coh}}{l_y \times l_z} \tag{5}$$

where *E(N)* is the total energy of the N atoms within a distance of 0.3 l_x to the GB plane, and E_{coh} represents the cohesive energy in the bulk system. l_y and l_z are the simulation box dimensions that multiply to represent the GB area.

The per-site segregation energy provides information on whether the substitution of the solute element is preferred on a specific atomic site. In this work, we focus on the sites at the GB region in the context of GB solute segregation. The per-site segregation energies on selected sites can be determined by calculating the energy difference between the system when a solute element X is located at the GB region and when it is in the bulk region. Therefore, by substituting one Mg atom with the solute atom in the GB region, the per-site segregation energies can be calculated according to Eq. (6):

$$E_{seg} = (E_{GB} + E_{bulk}^{X}) - (E_{GB}^{X} + E_{bulk}) \tag{6}$$

where E_{GB} is the energy of the structure with a GB, E_{GB}^{X} is the energy of the system when a Mg atom is substituted by a solute atom on a GB site. E_{bulk} and E_{bulk}^{X} denote the energy of the Mg bulk before and after the substitution of one solute atom, respectively. Here, the positive values denote that the solute atoms prefer to segregate on the GB sites. The Voronoi tessellation defines a volume centered at an atom and exclusively attributed to that atom [63,64], and was used to characterize the local atomic environments of the chosen GB sites. To better evaluate the performance of the selected potentials, the calculated segregation energies are compared with the density functional theory (DFT) results of Huber et al. [65] on the $\Sigma 7$ GB and Pei et al. [66] on the $\{10\bar{1}2\}$ tensile twin and $\{10\bar{1}1\}$ compression twin. To ensure consistency, the simulation samples were constructed with the same dimensions as the DFT models, including 180 atoms for the $\Sigma 7$ GB, 60 atoms for the $\{10\bar{1}2\}$ tensile twin, and 88 atoms for the $\{10\bar{1}1\}$ compression twin. It is important to note that PBC were applied to all three axes, which resulted in two GBs within the simulation domain. However, no elemental substitution took place at the second GB.

3. Results & discussion

3.1. Basic material properties

Bulk properties of the semi-empirical potentials were calculated, as shown in Table 1. All EAM and MEAM potentials demonstrate a good agreement with existing experimental data of lattice constants, cohesive energy and elastic tensors. Only the Pei_EAM potential exhibits significant deviations in C_{11} and C_{33} from the experimental values.

With respect to the computed formation energies of I_1 and I_2 basal stacking faults in Mg, only the Sheng_EAM potential exhibits unphysical negative values for basal SFEs. The hcp structure differs from the face-centered cubic (fcc) structure solely in their stacking sequence, with the stacking fault of the hcp structure being identical to the fcc structure. Consequently, the presence of negative SFE values implies that, under the Sheng_EAM potential, Mg is more stable in the fcc structure than in the hcp structure at the ground state, which is obviously incorrect.

For TBEs, a consistent trend is observed where the energy of the $\{10\bar{1}1\}$ compression twin is lower than that of the $\{10\bar{1}2\}$ tensile twin, aligning with the DFT results. However, this trend is reversed when applying the Wilson_EAM potential. Furthermore, an unrealistic twin structure is observed when applying Mendelev_EAM potential, which was also reported by Wu et al. [30].

Drawing from the outcomes of the potential benchmark on the basic material properties, we have narrowed down our selection of Mg potentials to four options that exhibit the least discrepancy with the experimental and DFT data. Further assessment of defect properties was performed using mainly the Kim_MEAM, Ahmad_MEAM, Dickel_MEAM and Liu_EAM potentials.

3.2. Generalized stacking fault energy and dislocation properties

The generalized stacking fault energy is a parameter that describes the slip behavior of crystalline materials. In this study, atomistic simulations were performed on the basal, prismatic, pyramidal I and II slip planes using selected pure Mg potentials to generate GSFE curves along specific directions, as shown in Fig. 1. For the first $\{10\bar{1}1\}$ and second order $\{11\bar{2}2\}$ pyramidal planes, our focus was on the $\{11\bar{2}3\}$ slip directions, given the importance of $\langle c + a \rangle$ slip in accommodating imposed plastic strains out of the basal plane [67–70]. The peak on the GSFE curve, known as unstable stacking fault energy (USFE), represents the energy barrier of the slip event, whereas the local minimum along the displacement vector corresponds to a stable SFE. For the GSFE curves on the basal plane, as shown in Fig. 1(a), all the potentials exhibit an overestimation of the energy barrier for basal slip when compared with the DFT results. As for the GSFE curves on the prismatic plane in Fig. 1(b), the USFE predicted using the Liu_EAM potential is much lower than the results obtained from both the MEAM potentials and DFT. Furthermore, a minor local minimum is observed at the center of the GSFE curves of all four potentials, which is not present on the DFT curve. This phenomenon can be an intrinsic artefact of the semi-empirical potentials, as highlighted by Stricker et al. [7]. Asymmetric GSFE curves about the local minimum are observed for the pyramidal I & II $\langle c + a \rangle$ slip systems, indicating a direction-dependent dislocation motion in the negative and positive slip directions on these two slip planes, as demonstrated in the following content on dislocation properties.

We further evaluated the performance of Mg potentials in the prediction of dislocation properties, including dislocation core structures and Peierls barriers. After the introduction of edge or screw dislocations onto the slip planes, the structures were relaxed to minimize the total energy, enabling the determination of the dislocation core structures.

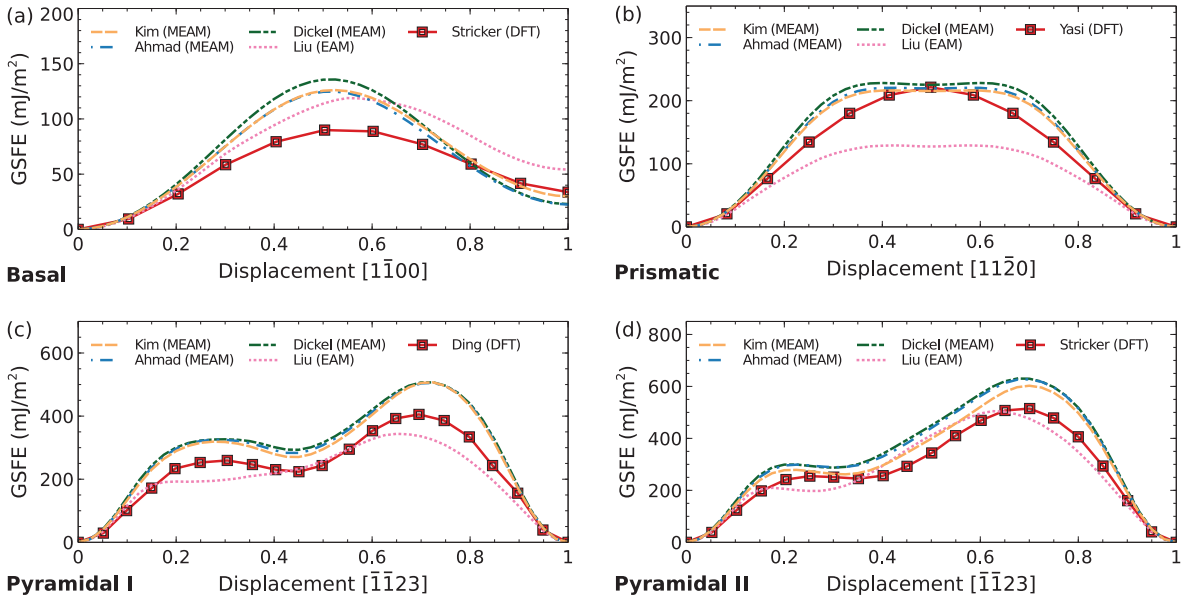

Fig. 1. GSFE curves on the basal (a), prismatic (b), pyramidal I (c) & II (d) slip planes of Ahmad_MEAM, Kim_MEAM, Dickel_MEAM, and Liu_EAM potentials in comparison with DFT results [7,25,34].

Table 2
Dislocation dissociation distance (expressed in terms of the lattice constant a) on the basal, prismatic, pyramidal I & II slip planes using Kim_MEAM, Ahmad_MEAM, Dickel_MEAM and Liu_EAM potentials, as compared to existing DFT results.

Slip plane	Basal		Prismatic		Pyramidal I		Pyramidal II	
Burgers vector	$\langle a \rangle$		$\langle a \rangle$		$\langle c+a \rangle$		$\langle c+a \rangle$	
Character	Edge	Screw	Edge	Screw	Edge	Screw	Edge	Screw
Kim_MEAM	9.2	3.0	1.0	1.0	9.2	4.1	5.1	3.4
Ahmad_MEAM	11.8	7.3	1.0	1.0	8.9	4.8	5.1	4.0
Dickel_MEAM	11.7	5.6	1.0	1.0	8.7	4.8	5.2	3.4
Liu_EAM	4.7	1.0	1.0	1.0	16.3	OPM	OPM	OPM
DFT results [30]	7.0	4.0	1.0	2.0	N/A	N/A	6.6	4.6

Table 3
Peierls stresses (in MPa) calculated using Kim_MEAM, Ahmad_MEAM, Dickel_MEAM and Liu_EAM potentials, as compared to existing experimental data.

Slip plane	Basal		Prismatic		Pyramidal I		Pyramidal II	
Burgers vector	$\langle a \rangle$		$\langle a \rangle$		$\langle c+a \rangle$		$\langle c+a \rangle$	
Character	Edge	Screw	Edge	Screw	Edge	Screw	Edge	Screw
Kim_MEAM	0.53	55	15	109	70 (63)	OPM (307)	204 (190)	294 (490)
Ahmad_MEAM	0.49	49	14	122	56 (75)	153 (353)	187 (246)	329 (617)
Dickel_MEAM	0.93	35	32	57	72 (54)	183 (200)	202 (202)	332 (400)
Liu_EAM	26.1	554	21	41	73 (96)	OPM (340)	OPM	OPM
Experimental results [70]	~ 0.5		~ 40		N/A		~ 40	

The dislocation core structures were visualized using the Nye tensor and differential displacement maps resolved in the direction of Burgers vectors, as shown in Fig. 2. The CNA method was applied to analyze the structure and determine the dislocation splitting distances, as presented in Table 2. The unit of the splitting distance is based on the lattice constant a. It is noteworthy that for the Liu_EAM potential, the $\langle c+a \rangle$ screw dislocation on the pyramidal I plane is not stable, along with the $\langle c+a \rangle$ edge and screw dislocations on the pyramidal II plane. The dislocation core structures dissociate from the slip plane after energy minimization. This phenomenon is referred to as an out-of-plane mechanism (OPM). The other three MEAM potentials generally exhibit similar behavior, and there is no significant deviation from the DFT results, except for the $\langle a \rangle$ screw dislocation on the prismatic plane, where the DFT data shows a more stable $\langle a \rangle$ screw dislocation on the basal plane [7,71]. This discrepancy is also connected to the artefact introduced by the potentials, as the stability and structure of the prismatic dislocations are highly related to the previously observed local minimum on the prismatic GSFE curve [7].

The calculated Peierls stresses, using the quasi-static method, are listed in Table 3. Compared with the MEAM potentials and experimental results, the Peierls stress of the Liu_EAM potential is significantly higher for both edge and screw dislocations on the basal plane. Due to the direction-dependent energy profile of $\langle c+a \rangle$ slip on the pyramidal I and II planes, as mentioned earlier, there are two Peierls barriers associated with these two planes. Similarly, the Liu_EAM potential failed to predict the Peierls stress for most of the dislocations on these two planes due to the out-of-plane mechanism. This phenomenon is also observed in the $\langle c+a \rangle$ screw dislocation on the pyramidal I plane using the Kim_MEAM potential, where the screw dislocation cross-slips to the pyramidal II slip plane. In general, all three evaluated MEAM potentials can provide reliable predictions of dislocation properties, whereas the Liu_EAM potential leads to unrealistic $\langle c+a \rangle$ dislocation core structures and Peierls stresses.

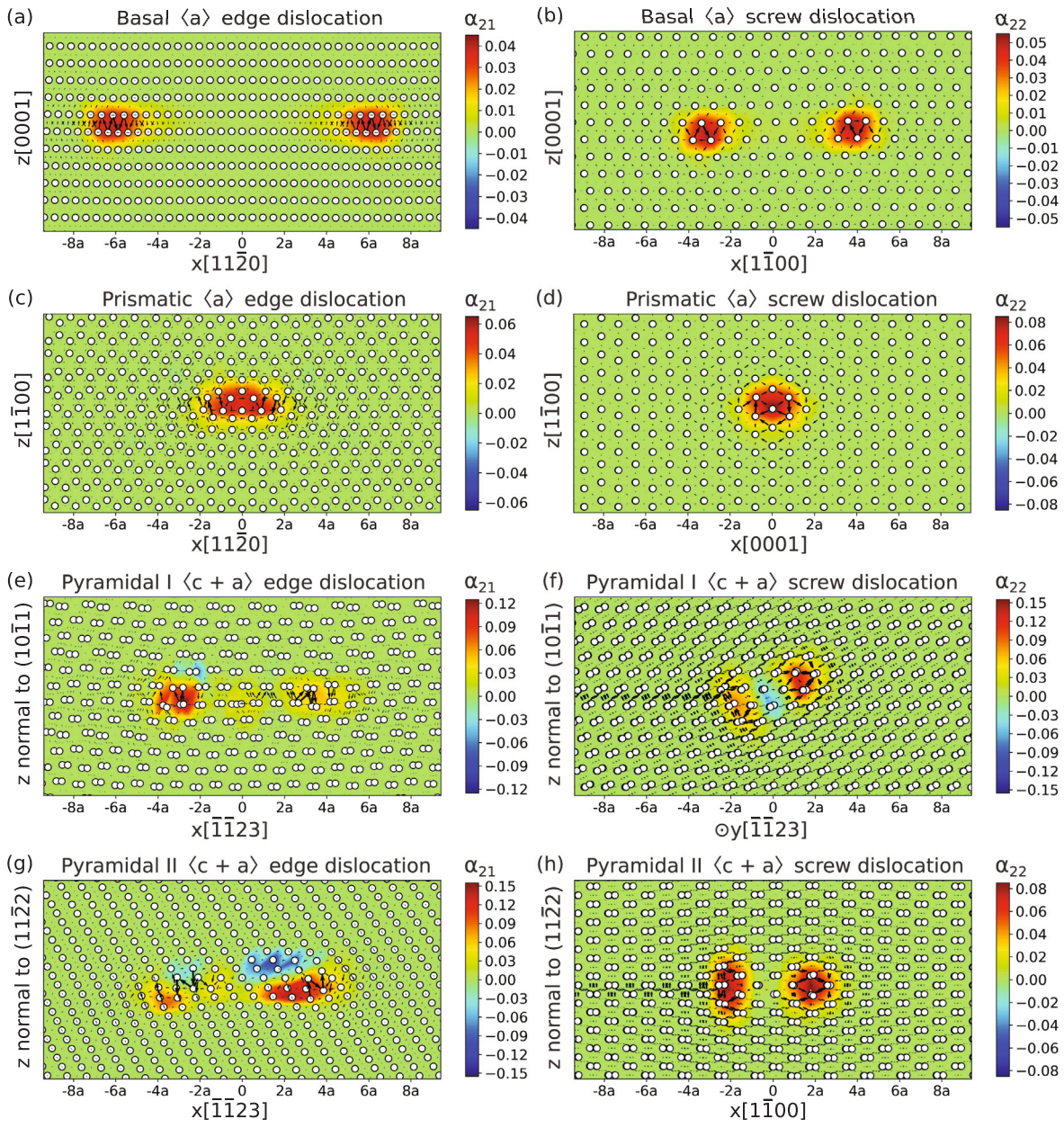

Fig. 2. Dislocation core structures visualized by the component of the Nye tensor and differential displacement maps along the direction of Burgers vector using the Ahmad_MEAM potential. (a) Basal ⟨*a*⟩ edge, (b) basal ⟨*a*⟩ screw, (c) prismatic ⟨*a*⟩ edge, (d) prismatic ⟨*a*⟩ screw, (e) pyramidal I ⟨*c* + *a*⟩ edge, (f) pyramidal I ⟨*c* + *a*⟩ screw, (g) pyramidal II ⟨*c* + *a*⟩ edge, and (h) pyramidal II ⟨*c* + *a*⟩ screw dislocations.

Table 4
Calculated Σ7 GB energy and structure of tested potentials for pure Mg in comparison with existing DFT results.

Potentials	Kim_MEAM	Ahmad_MEAM	Dickel_MEAM	Liu_EAM	Wilson_EAM	Mendelev_EAM	Pei_EAM	Sheng_EAM	DFT results [65]
$E_{GB}^{\Sigma 7}$ (mJ/m^2)	335	346	354	254/259	329	316	340	303	299/298 (A/T)
Σ7 Type	T-type	T-type	T-type	A/T-type	A-like type	A-type	A-like type	A-like type	A/T-type

3.3. Grain boundary energies

In Section 3.1 we evaluated the performance of the Mg potentials with respect to planar defect properties, including SFEs and TBEs. Here, we extend this investigation to the ⟨0001⟩ symmetric tilt GBs. The properties of the Σ7 GB were investigated first to facilitate a meaningful comparison with the DFT study by Huber et al. [65]. By using the same atomic configuration, we aimed to conduct a comparable assessment of the Mg potentials. The calculated properties are presented in Table 4. Notably, the GB energies of the Σ7 GB display good agreement with the DFT results for all potentials. As detailed in [72], two types of GB structures with the same macroscopic characters but different microscopic degrees of freedom exist, namely A-type and T-type, distinguished by their dislocation core configurations. However, in our study, we found that only the T-type grain boundary remained stable at 0 K for the MEAM potentials, while the A-type grain boundary remained stable exclusively for the EAM potentials. An exception arises when applying the Liu_EAM potential, as both A-type and T-type GBs can be stabilized after energy minimization. Despite these different trends, the comparison of GB energies reveals that the A-type GB possesses

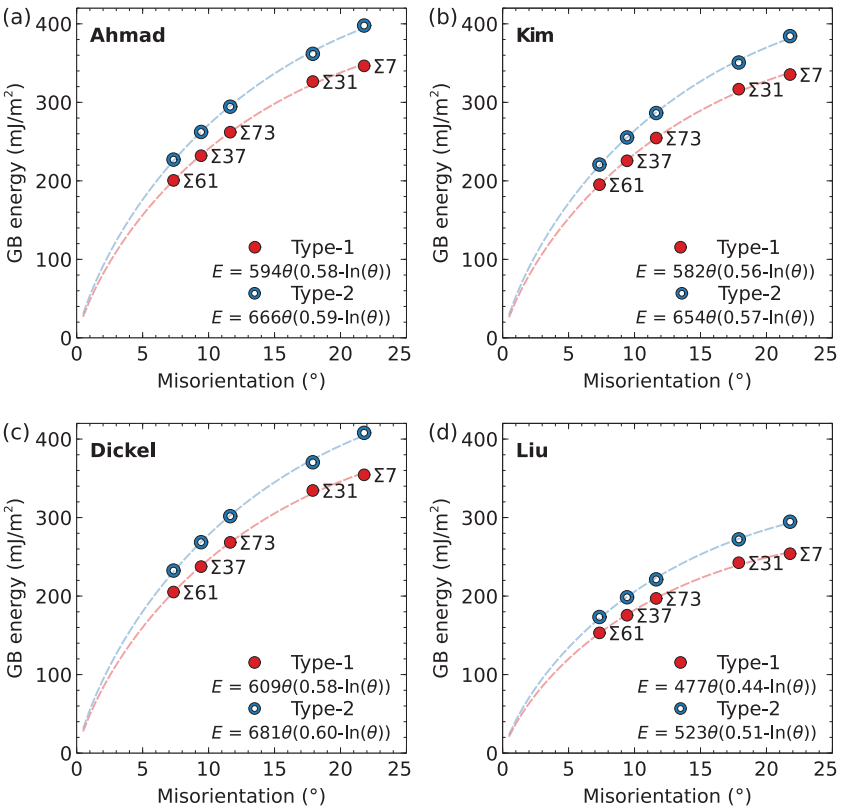

Fig. 3. GB energies of five pairs of type-1 and type-2 <0001> symmetric tilt CSL GBs computed using: (a) Ahmad_MEAM, (b) Kim_MEAM, (c) Dickel_MEAM, (d) Liu_EAM potentials. The misorientation on the x-axis refers to the type-1 GBs, that is the θ angle. The misorientaiton ϕ for the type-2 GBs is obtained by $\phi = 60° - \theta$.

lower energy, suggesting that it is more stable when employing EAM potentials. Additionally, for the Wilson_EAM, Pei_EAM, and Sheng_EAM potentials, the geometry of the $\Sigma 7$ GB deviates slightly from the A-type GB observed in DFT, which is indicated in the following by referring to it as A-like type.

To investigate the $\langle 0\,0\,0\,1\rangle$ symmetric tilt GBs in the current study, we selected five pairs of CSL GBs, including $\Sigma 61$, $\Sigma 37$, $\Sigma 73$, $\Sigma 31$ and $\Sigma 7$. For each Σ value, there are two GBs depending on the tilt angle, which is defined as twice the dihedral angle between the GB plane and $\{1\,1\,\bar{2}\,0\}$. The one with the smaller tilt angle θ is referred to as type-1, while the one with the larger tilt angle ϕ is referred to as type-2. It should be noted that, due to the symmetry of the hcp structure, the sum of θ and ϕ is equal to 60°. A detailed description of the classification of type-1 and type-2 GBs, along with the list of tilt angles for the selected CSL GBs, can be found in [21]. Using the selected Mg potentials, the GB energies of these five pairs of CSL GBs were calculated, as shown in Fig. 3. It is noticeable that the calculated GB energies using the Liu_EAM potential are lower than the other three calculations using MEAM potentials. Irrespective of the potential applied, the energies of type-1 GBs are lower than those of type-2 GBs. This result correlates well with the experimental observation, where a predominance of type-1 GBs in a basal-textured Mg thin film was found [21]. Additionally, for all four potentials, the GB energies fit well to the following formula for low-angle GBs, as shown in Fig. 3.

$$E_{\mathrm{GB}}(\theta) = E_0\theta(A - ln(\theta)) \tag{7}$$

where θ is in radian. E_0 and A are fitting parameters, where E_0 has the same unit as E_{GB} (mJ/m^{-2}) and A is dimensionless. It is noticeable that regardless of the potential employed or the GB type, the fitted A parameter consistently converges to similar values around 0.5, and the fitted E_0 values are consistently higher for MEAM potentials compared to the EAM potential. The observed good fit suggests that this dislocation model for low-angle GBs is applicable to both type-1 and type-2 GBs irrespective of the employed potential.

3.4. Segregation energies

The preceding sections demonstrate the performance of the selected potentials for pure Mg. To extend the assessment of their predictive capabilities to solute-related properties in Mg alloys, the focus now shifts towards assessing their performance in predicting GB segregation energies. Three MEAM and two EAM potentials with Mg-X interactions were chosen: Kim_MEAM (Mg–Y, Mg–Zn, Mg–Al, Mg–Nd), Ahmad_MEAM (Mg–Y), Dickel_MEAM (Mg–Zn), Liu_EAM (Mg–Al), and Mendelev_EAM (Mg–Al). Using Eq. (6), atomistic simulations were applied to calculate the per-site segregation energies of selected GB sites on the $\Sigma 7$ GB, $\{1\,0\,\bar{1}\,1\}$ compression twin (CT) and $\{1\,0\,\bar{1}\,2\}$ tensile twin (TT) boundaries, where positive values indicate that the alloying element has a preference for segregation to those specific sites in the GB. For the $\Sigma 7$ GBs, the selected sites are marked based on the distance to the GB (see Figs. 4 and 5). For the CT and TT, two sites on the TB are selected, as shown in Fig. 4.

The segregation energies of GB sites demonstrate a good correlation with local atomic environments. In addition, all tested MEAM and EAM potentials show good agreement with the DFT calculations, as shown in Figs. 4 and 5. We quantified the change in local atomic environments at the GBs by comparing the atomic volumes of the GB sites with that of the bulk site, as shown in Table 5. For instance, regardless of the potential, the atomic volume of the A (or A1) site at the TB is smaller than that of the site in the bulk, whereas the atomic volume of the B (or B1) site is larger. By integrating the findings from Figs. 4 and 5, a clear trend emerges. Y and Nd atoms exhibit a pronounced inclination to segregate towards the B-sites with comparatively larger atomic volumes. In contrast, Zn and Al atoms manifest a propensity for the A-sites. This observation aligns with the nature of the stress field generated by the substitution atom. To confirm this, we calculated the volume change resulting from the substitution of a single solute atom in a bulk sample containing 5 × 5 × 5 unit cells. The results are listed

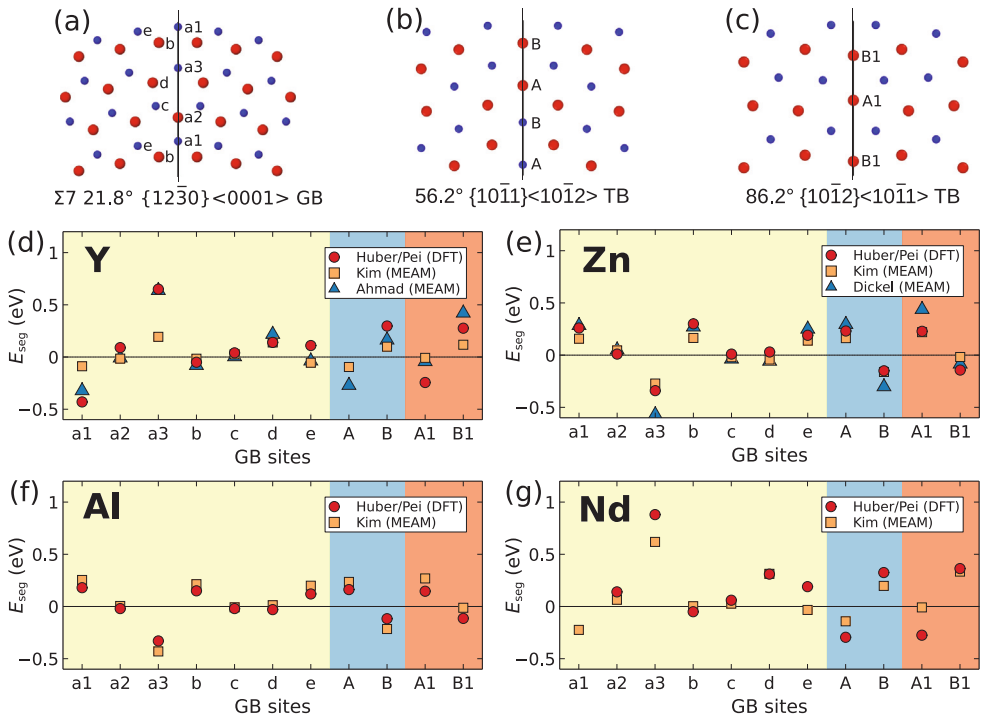

Fig. 4. Selected GB sites from (a) T-type Σ7 GB (a1, a2, a3, b, c, d, and e sites), (b) {10$\bar{1}$1} TB (A and B sites), and (c) {10$\bar{1}$2} TB (A1 and B1 sites), along with the corresponding per-site segregation energies in binary Mg-X alloys for (d) Y, (e) Zn, (f) Al, and (g) Nd solutes using selected Mg MEAM potentials in comparison with existing DFT data [65,66]. The background colors are assigned according to the types of GBs: Σ7 GB is highlighted in yellow, {10$\bar{1}$1} TB in blue, and {10$\bar{1}$2} TB in orange.

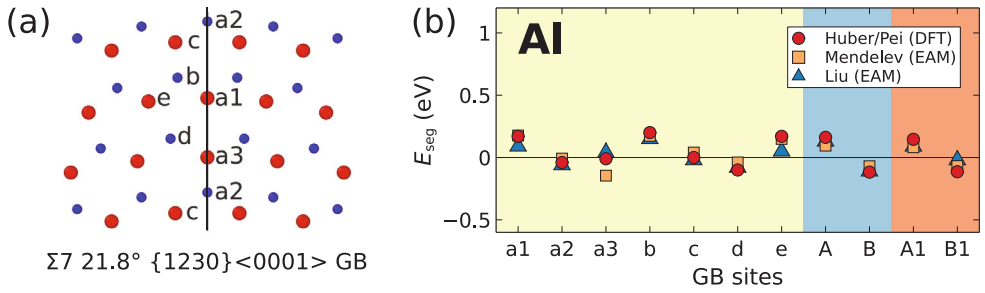

Fig. 5. (a) GB sites in A-type Σ7 GB . (b) Per-site segregation energies in binary Mg alloys for Al solute at A-type Σ7 GB (a1, a2, a3, b, c, d, and e sites), {10$\bar{1}$1} TB (A and B sites), and {10$\bar{1}$2} TB (A1 and B1 sites), along with the corresponding using Mg EAM potentials in comparison with existing DFT data [65,66]. The background colors are assigned according to the types of GBs: Σ7 GB is highlighted in yellow, {10$\bar{1}$1} TB in blue, and {10$\bar{1}$2} TB in orange.

Table 5
Variation of atomic volume of the selected GB sites in Fig. 4 as compared to the bulk site using different potentials. The label *(A)* indicates that the Σ7 GB exhibits an A-type structure using Liu_EAM and Mendelev_EAM potentials, while the rest of the entries for the Σ7 GB pertain to T-type structures.

Site	Kim_MEAM	Ahmad_MEAM	Dickel_MEAM	Liu_EAM	Mendelev_EAM
Σ7 a1	−4.5%	−4.7%	−4.8%	0.0% *(A)*	0.1% *(A)*
Σ7 a2	0.4%	0.3%	0.5%	0.3% *(A)*	0.6% *(A)*
Σ7 a3	18.4%	18.3%	18.8%	6.4% *(A)*	8.0% *(A)*
Σ7 b	−0.3%	−0.5%	−0.6%	−4.7% *(A)*	−4.8% *(A)*
Σ7 c	0.9%	1.0%	1.2%	−1.0% *(A)*	−2.1% *(A)*
Σ7 d	6.7%	6.8%	7.1%	12.2% *(A)*	12.4% *(A)*
Σ7 e	−1.5%	−1.4%	−1.2%	−2.3% *(A)*	−2.3% *(A)*
CT A	−3.6%	−3.5%	−3.5%	−3.5%	−3.5%
CT B	5.1%	5.0%	5.0%	4.1%	4.5%
TT A1	−5.8%	−5.8%	−5.9%	−6.9%	−5.2%
TT B1	8.1%	8.1%	8.4%	7.3%	2.7%

in Table 6, where positive values indicate that the solute atom generates a compressive stress field within the local atomic environment, while negative values correspond to a tensile stress field. Evidently, elements inducing a compressive stress field, such as Y and Nd, prefer to segregate at sites with larger atomic volumes. Conversely, elements leading to a tensile stress field tend to segregate at smaller sites. When the atomic volume of a site is close to that of the bulk, the computed segregation energies are close to zero. This direct correlation between the per-site segregation energies and the atomic volume of the sites can be attributed to the minimization of elastic strain energy due to atomic

Table 6
Atomic volume change ΔV (in $Å^3$) by the substitution of a single solute atom in a bulk sample containing 5 × 5 × 5 unit cells and per-site segregation energies (in eV) of solute elements (Y, Zn, Ca, Sn, Li, Al, Nd, Pb) at the selected GB sites in Mg. The bold values indicate a structural transformation by introducing a solute atom after energy minimization. The label *(A)* indicates that the Σ7 GB exhibits an A-type structure using Liu_EAM and Mendelev_EAM potentials, while the remaining entries of Σ7 GB correspond to T-type structures.

Site	Y_Kim	Y_Ahmad	Zn_Kim	Zn_Dickel	Ca_Kim	Sn_Kim	Li_Kim	Al_Kim	Al_Liu	Al_Mendelev	Nd_Kim	Pb_Kim
ΔV	5.56	13.51	−7.42	−12.14	13.92	6.40	−3.05	−6.99	−8.73	−7.95	16.17	−4.31
Σ7 a1	−0.09	−0.32	0.16	0.28	−0.21	−0.16	0.14	0.25	0.09 *(A)*	0.18 *(A)*	−0.22	0.11
Σ7 a2	−0.02	−0.01	0.05	0.05	−0.04	−0.15	0.00	0.01	−0.06 *(A)*	−0.01 *(A)*	0.06	−0.07
Σ7 a3	0.19	0.64	−0.27	−0.57	0.40	−0.08	−0.03	−0.43	0.04 *(A)*	−0.15 *(A)*	0.62	−0.04
Σ7 b	−0.02	−0.08	0.16	0.27	**−0.05**	**−0.20**	0.23	0.21	0.15 *(A)*	0.17 *(A)*	**0.00**	**0.30**
Σ7 c	0.03	0.00	−0.02	−0.04	0.08	0.10	0.01	−0.01	−0.02 *(A)*	0.04 *(A)*	0.03	0.09
Σ7 d	**0.14**	**0.22**	−0.04	−0.06	0.20	0.08	**0.08**	**0.01**	−0.08 *(A)*	**−0.04** *(A)*	**0.31**	**0.13**
Σ7 e	−0.05	**−0.04**	0.14	0.25	**−0.03**	−0.20	**0.11**	**0.20**	**0.05** *(A)*	0.15 *(A)*	**−0.03**	**0.13**
CT A	−0.10	−0.27	0.16	0.29	−0.18	−0.04	0.13	0.24	0.13	0.10	−0.14	0.21
CT B	0.10	0.16	−0.16	−0.30	0.19	0.07	−0.05	−0.22	−0.11	−0.07	0.20	−0.21
TT A1	**−0.01**	**−0.04**	0.22	0.44	**0.00**	**−0.04**	0.20	0.27	0.09	0.08	**−0.01**	−0.02
TT B1	0.12	0.42	**−0.02**	−0.09	0.25	0.17	−0.06	**−0.01**	**−0.02**	**−0.07**	0.33	0.01

size mismatch. Apart from the lattice mismatching effect, the reduction of the interfacial energy and enthalpy of mixing (ΔH_{mix}) can also act as driving forces for segregation dynamics. The contribution of interfacial energy reduction is limited for the simulated highly symmetric GBs due to their low-energy nature. In contrast, the chemical driving force from ΔH_{mix} between solvent and solute is not negligible, especially when compared to the range of segregation energies, e.g., ΔH_{mix} equals 0.08 and 0.05 eV/atom for the Mg–Al system using the Kim_MEAM and Liu_EAM potentials, respectively. Furthermore, the influence of chemical bonding, encompassing coordination environment and solute electronic configuration, can lead to unusual solute segregation behavior in twin boundaries for specific elements [73]. For instance, Bi with a larger atomic radius than that of Mg is found to segregate to the compression site in compression twin boundaries but not to any sites in the tensile twin boundaries [73]. Such chemical bonding effects might be beyond the capability of semi-empirical potentials, such as EAM and MEAM, therefore require electronic structure calculations.

In general, all selected MEAM and EAM potentials show good performance in predicting the segregation energies compared to the DFT results [65,66], as shown in Figs. 4 and 5. However, it is important to note that some of the substitutional sites, as indicated in bold values in Table 6, experience a transformation in the local atomic environment after relaxation, as characterized using the CNA method. Moreover, the sites experiencing the transformation differ between the interatomic potentials and the DFT calculations, contributing to some of the observed discrepancies in the segregation energies. Indeed, this solute segregation-induced structural transformation has been observed in experiments, as reported by Mathews et al. [74] in their study of Ga-decorated Σ7 GBs in Mg. To more comprehensively illustrate the relationship between the per-site segregation energies of alloying elements and the excess free volumes at GBs, we extended our calculations to additional alloying elements at selected GB sites. All the results are presented in Table 6. Note that when using MEAM potentials, the Σ7 GB remains stable only in the T-type configuration. In contrast, Liu_EAM and Mendelev_EAM potentials favor the A-type configuration, leading to the selection of different GB sites.

The per-site segregation energies obtained in this work can be used to predict solute concentrations at these GBs using the Langmuir–McLean segregation isotherm in the context of infinitesimally diluted systems [75,76]. It is worth noting that at high concentration levels, the consideration of solute-solute interactions becomes crucial, which highlights the importance of calculations of co-segregation energies. Future investigations of segregation in Mg alloys should extend their focus to more general GBs, like those in polycrystalline materials. This is because the extensively studied highly-symmetric GBs using DFT may not adequately capture the wide spectrum of GB local atomic environments, ultimately leading to incorrect predictions in structure–property relationship [77].

4. Conclusions

A variety of commonly employed EAM and MEAM potentials for Mg and its alloys was applied in atomistic simulations to compute defect characteristics, including dislocation properties, grain boundary energies, and segregation energies. Conducting a thorough comprehensive comparison with available experimental and DFT data enabled a systematic assessment of these semi-empirical interatomic potentials. From the obtained results, the following conclusions can be inferred:

- The assessment of selected potentials in predicting various basic material properties revealed excellent agreement with available experimental data. However, Pei_EAM, Sheng_EAM, Wilson_EAM and Mendelev_EAM potentials showed inconsistencies in certain properties, such as the stacking fault energy and the structure and energy of twin boundaries.
- When using Liu_EAM, Kim_MEAM, Ahmad_MEAM and Dickel_MEAM potentials to analyze the generalized stacking fault energy curves, the energy barrier for basal slip was overestimated in comparison to DFT data. In addition, an unexpected local minimum was evident for the prismatic slip system, which can be linked to the presence of a stable $\langle a \rangle$ screw dislocation on the prismatic plane, in contradiction to DFT results.
- Regarding the computed dislocation properties, the three MEAM potentials exhibit excellent agreement with DFT calculations. Conversely, the Liu_EAM potential results in unrealistic $\langle c + a \rangle$ dislocation core structures and Peierls stresses.
- In the context of $\langle 0\,0\,0\,1 \rangle$ symmetric tilt GBs, the formation energies of type-1 GBs are consistently lower than those of type-2 GBs. Regardless of the potential used, the dislocation model for low-angle GBs proved applicable to both types of GBs. With respect to the Σ7 GB, the choice of potential significantly influences its structural type; T-type and A-type structures are stable for MEAM and EAM potentials, respectively.
- Per-site segregation energies of a wide range of alloying elements at Σ7 GB and twin boundaries were calculated. All tested EAM and MEAM potentials show good agreement with the DFT calculations. A strong correlation between the segregation energies and the local atomic environment was observed for all potentials, highlighting the significance of the minimization of elastic strain energy due to atomic size mismatch on solute segregation behavior.

CRediT authorship contribution statement

Hexin Wang: Writing – original draft, Investigation. **Julien Guénolé:** Writing – review & editing, Conceptualization. **Sandra Korte-Kerzel:** Writing – review & editing, Supervision. **Talal Al-Samman:** Writing – review & editing, Supervision, Funding acquisition. **Zhuocheng Xie:** Writing – review & editing, Supervision, Funding acquisition, Conceptualization.

Declaration of competing interest

The authors declare that they have no known competing financial interests or personal relationships that could have appeared to influence the work reported in this paper.

Data availability

Data will be made available on request.

Acknowledgments

H.W., Z.X. and T.A.S. acknowledge the financial support by the German Research Foundation (DFG) (Grant Nr. 505716422). T.A.S. are grateful for the financial support from the DFG (Grant Nr. AL1343/7-1, AL1343/8-1 and Yi 103/3-1). Z.X. and S.K.K. acknowledge financial support by the DFG through the projects A02, A05 and C02 of the SFB1394 Structural and Chemical Atomic Complexity – From Defect Phase Diagrams to Material Properties, project ID 409476157. Additionally, Z.X. and S.K.K. are grateful for funding from the European Research Council (ERC) under the European Union's Horizon 2020 research and innovation programme (grant agreement No. 852096 FunBlocks). J.G. acknowledges funding from the French National Research Agency (ANR), Grant ANR-21-CE08-0001 (ATOUUM) and ANR-22-CE92-0058-01 (SILA). The authors gratefully acknowledge the computing time provided to them at the NHR Center NHR4CES at RWTH Aachen University (project number p0020431). This is funded by the Federal Ministry of Education and Research, and the state governments participating on the basis of the resolutions of the GWK for national high performance computing at universities (www.nhr-verein.de/unsere-partner).

References

[1] T.M. Pollock, Weight loss with magnesium alloys, Science 328 (5981) (2010) 986–987.
[2] E. Kelley, The deformation characteristics of textured magnesium, Trans. Metall. Soc. AIME 242 (1968) 654–660.
[3] S. Sandlöbes, M. Friák, S. Zaefferer, A. Dick, S. Yi, D. Letzig, Z. Pei, L.-F. Zhu, J. Neugebauer, D. Raabe, The relation between ductility and stacking fault energies in Mg and Mg–Y alloys, Acta Mater. 60 (2012) 3011–3021.
[4] B. Yin, Z. Wu, W. Curtin, First-principles calculations of stacking fault energies in Mg–Y, Mg–Al and Mg-Zn alloys and implications for <c+a> activity, Acta Mater. 136 (2017) 249–261.
[5] J. Zhang, Y. Zhang, J.A. El-Awady, Y. Tang, The plausibility of <c+a> dislocation slip on $\{\bar{1}2\bar{1}1\}$ planes in Mg, Scr. Mater. 156 (2018) 19–22.
[6] V. Yamakov, D. Wolf, S.R. Phillpot, A.K. Mukherjee, H. Gleiter, Dislocation processes in the deformation of nanocrystalline aluminium by molecular-dynamics simulation, Nat. Mater. 1 (1) (2002) 45–49.
[7] M. Stricker, B. Yin, E. Mak, W. Curtin, Machine learning for metallurgy II. A neural-network potential for magnesium, Phys. Rev. Mater. 4 (10) (2020) 103602.
[8] E. Bitzek, P. Gumbsch, Dynamic aspects of dislocation motion: Atomistic simulations, Mater. Sci. Eng. A 400 (2005) 40–44.
[9] Z. Trautt, Y. Mishin, Grain boundary migration and grain rotation studied by molecular dynamics, Acta Mater. 60 (5) (2012) 2407–2424.
[10] N. Kheradmand, H. Vehoff, A. Barnoush, An insight into the role of the grain boundary in plastic deformation by means of a bicrystalline pillar compression test and atomistic simulation, Acta Mater. 61 (19) (2013) 7454–7465.
[11] A. Hasnaoui, P. Derlet, H. Van Swygenhoven, Interaction between dislocations and grain boundaries under an indenter–A molecular dynamics simulation, Acta Mater. 52 (8) (2004) 2251–2258.
[12] R. Pei, Z. Xie, S. Yi, S. Korte-Kerzel, J. Guénolé, T. Al-Samman, Atomistic insights into the inhomogeneous nature of solute segregation to grain boundaries in magnesium, Scr. Mater. 230 (2023) 115432.
[13] P.C. Millett, R.P. Selvam, A. Saxena, Molecular dynamics simulations of grain size stabilization in nanocrystalline materials by addition of dopants, Acta Mater. 54 (2) (2006) 297–303.
[14] L. Karkina, I. Karkin, A. Kuznetsov, I. Razumov, P.A. Korzhavyi, Y.N. Gornostyrev, Solute–grain boundary interaction and segregation formation in Al: First principles calculations and molecular dynamics modeling, Comput. Mater. Sci. 112 (2016) 18–26.
[15] M.S. Daw, M.I. Baskes, Embedded-atom method: Derivation and application to impurities, surfaces, and other defects in metals, Phys. Rev. B 29 (12) (1984) 6443.
[16] M.I. Baskes, Modified embedded-atom potentials for cubic materials and impurities, Phys. Rev. B 46 (5) (1992) 2727.
[17] X.-Y. Liu, J.B. Adams, Grain-boundary segregation in Al–10% Mg alloys at hot working temperatures, Acta Mater. 46 (10) (1998) 3467–3476.
[18] Y.-J. Hu, V. Menon, L. Qi, Formation of I1 stacking fault by deformation defect evolution from grain boundaries in Mg, J. Magnes. Alloys 10 (10) (2022) 2717–2729.
[19] Z. Li, J. Wang, W. Liu, Basal <a> dislocation-$\{\bar{1}011\}$ contraction twin interactions in magnesium, Comput. Mater. Sci. 155 (2018) 11–16.
[20] G. Zu, S. Groh, Effect of segregated alloying element on the intrinsic fracture behavior of Mg, Theor. Appl. Fract. Mech. 85 (2016) 236–245.
[21] S. Zhang, Z. Xie, P. Keuter, S. Ahmad, L. Abdellaoui, X. Zhou, N. Cautaerts, B. Breitbach, S. Aliramaji, S. Korte-Kerzel, et al., Atomistic structures of <0001> tilt grain boundaries in a textured Mg thin film, Nanoscale 14 (48) (2022) 18192–18199.
[22] T. Nogaret, W. Curtin, J. Yasi, L. Hector Jr., D. Trinkle, Atomistic study of edge and screw <c+a> dislocations in magnesium, Acta Mater. 58 (13) (2010) 4332–4343.
[23] D. Sun, M. Mendelev, C. Becker, K. Kudin, T. Haxhimali, M. Asta, J. Hoyt, A. Karma, D.J. Srolovitz, Crystal-melt interfacial free energies in HCP metals: A molecular dynamics study of Mg, Phys. Rev. B 73 (2) (2006) 024116.
[24] S. Groh, E. Marin, M. Horstemeyer, D. Bammann, Dislocation motion in magnesium: A study by molecular statics and molecular dynamics, Modelling Simul. Mater. Sci. Eng. 17 (7) (2009) 075009.
[25] J. Yasi, T. Nogaret, D. Trinkle, Y. Qi, L. Hector, W. Curtin, Basal and prism dislocation cores in magnesium: Comparison of first-principles and embedded-atom-potential methods predictions, Modelling Simul. Mater. Sci. Eng. 17 (5) (2009) 055012.
[26] Y. Tang, J.A. El-Awady, Formation and slip of pyramidal dislocations in hexagonal close-packed magnesium single crystals, Acta Mater. 71 (2014) 319–332.
[27] T. Tang, S. Kim, M.F. Horstemeyer, P. Wang, Atomistic modeling of crack growth in magnesium single crystal, Eng. Fract. Mech. 78 (1) (2011) 191–201.
[28] T. Tang, S. Kim, M.F. Horstemeyer, P. Wang, A molecular dynamics study of fracture behavior in magnesium single crystal, in: Magnesium Technology 2011, Springer, 2016, pp. 349–355.
[29] K.-H. Kim, J.B. Jeon, B.-J. Lee, Modified embedded-atom method interatomic potentials for Mg–X (X=Y, Sn, Ca) binary systems, CALPHAD 48 (2015) 27–34.
[30] Z. Wu, M. Francis, W. Curtin, Magnesium interatomic potential for simulating plasticity and fracture phenomena, Modelling Simul. Mater. Sci. Eng. 23 (1) (2015) 015004.
[31] H. Fan, Q. Wang, X. Tian, J.A. El-Awady, Temperature effects on the mobility of pyramidal <c+a> dislocations in magnesium, Scr. Mater. 127 (2017) 68–71.
[32] H. Fan, J. Tang, X. Tian, Q. Wang, X. Tian, J.A. El-Awady, Core structures and mobility of <c> dislocations in magnesium, Scr. Mater. 135 (2017) 37–40.
[33] C.D. Barrett, A. Imandoust, H. El Kadiri, The effect of rare earth element segregation on grain boundary energy and mobility in magnesium and ensuing texture weakening, Scr. Mater. 146 (2018) 46–50.
[34] Z. Ding, W. Liu, H. Sun, S. Li, D. Zhang, Y. Zhao, E.J. Lavernia, Y. Zhu, Origins and dissociation of pyramidal <c+a> dislocations in magnesium and its alloys, Acta Mater. 146 (2018) 265–272.
[35] Z. Wu, W. Curtin, Brittle and ductile crack-tip behavior in magnesium, Acta Mater. 88 (2015) 1–12.
[36] Y. Sato, T. Swinburne, S. Ogata, D. Rodney, Anharmonic effect on the thermally activated migration of $\{10\bar{1}2\}$ twin interfaces in magnesium, Mater. Res. Lett. 9 (5) (2021) 231–238.
[37] A.P. Thompson, H.M. Aktulga, R. Berger, D.S. Bolintineanu, W.M. Brown, P.S. Crozier, P.J. in't Veld, A. Kohlmeyer, S.G. Moore, T.D. Nguyen, et al., LAMMPS-a flexible simulation tool for particle-based materials modeling at the atomic, meso, and continuum scales, Comput. Phys. Comm. 271 (2022) 108171.
[38] E. Bitzek, P. Koskinen, F. Gähler, M. Moseler, P. Gumbsch, Structural relaxation made simple, Phys. Rev. Lett. 97 (17) (2006) 170201.
[39] J. Guénolé, W.G. Nöhring, A. Vaid, F. Houllé, Z. Xie, A. Prakash, E. Bitzek, Assessment and optimization of the fast inertial relaxation engine (FIRE) for energy minimization in atomistic simulations and its implementation in lammps, Comput. Mater. Sci. 175 (2020) 109584.
[40] S. Wilson, M. Mendelev, A unified relation for the solid-liquid interface free energy of pure FCC, BCC, and HCP metals, J. Chem. Phys. 144 (14) (2016) 144707.
[41] M. Mendelev, M. Asta, M. Rahman, J. Hoyt, Development of interatomic potentials appropriate for simulation of solid–liquid interface properties in Al–Mg alloys, Phil. Mag. 89 (34–36) (2009) 3269–3285.
[42] Z. Pei, H. Sheng, X. Zhang, R. Li, B. Svendsen, Tunable twin stability and an accurate magnesium interatomic potential for dislocation-twin interactions, Mater. Des. 153 (2018) 232–241.
[43] H. Sheng, https://sites.google.com/site/eampotentials/.

[44] R. Ahmad, S. Groh, M. Ghazisaeidi, W.A. Curtin, Modified embedded-atom method interatomic potential for Mg–Y alloys, Modelling Simul. Mater. Sci. Eng. 26 (6) (2018) 065010.

[45] D.E. Dickel, M.I. Baskes, I. Aslam, C.D. Barrett, New interatomic potential for Mg–Al–Zn alloys with specific application to dilute Mg-based alloys, Model. Simul. Mater. Sci. Eng. 26 (4) (2018) 045010.

[46] Y.-M. Kim, N.J. Kim, B.-J. Lee, Atomistic modeling of pure Mg and Mg–Al systems, CALPHAD 33 (4) (2009) 650–657.

[47] Y.-M. Kim, I.-H. Jung, B.-J. Lee, Atomistic modeling of pure Li and Mg–Li system, Modelling Simul. Mater. Sci. Eng. 20 (3) (2012) 035005.

[48] K.-H. Kim, B.-J. Lee, Modified embedded-atom method interatomic potentials for Mg-Nd and Mg-Pb binary systems, CALPHAD 57 (2017) 55–61.

[49] H.-S. Jang, K.-M. Kim, B.-J. Lee, Modified embedded-atom method interatomic potentials for pure Zn and Mg-Zn binary system, CALPHAD 60 (2018) 200–207.

[50] P. Hirel, Atomsk: A tool for manipulating and converting atomic data files, Comput. Phys. Comm. 197 (2015) 212–219.

[51] A. Vaid, E. Bitzek, S. Nasiri, M. Zaiser, et al., Pinning of extended dislocations in atomically disordered crystals, Acta Mater. 236 (2022) 118095.

[52] J.D. Honeycutt, H.C. Andersen, Molecular dynamics study of melting and freezing of small Lennard-Jones clusters, J. Phys. Chem. 91 (19) (1987) 4950–4963.

[53] A. Stukowski, Visualization and analysis of atomistic simulation data with OVITO–the open visualization tool, Model. Simul. Mater. Sci. Eng. 18 (1) (2009) 015012.

[54] C. Hartley, Y. Mishin, Characterization and visualization of the lattice misfit associated with dislocation cores, Acta Mater. 53 (5) (2005) 1313–1321.

[55] V. Vitek, R. Perrin, D. Bowen, The core structure of $1/2$ (111) screw dislocations in BCC crystals, Phil. Mag. 21 (173) (1970) 1049–1073.

[56] E. Clouet, D. Caillard, N. Chaari, F. Onimus, D. Rodney, Dislocation locking versus easy glide in titanium and zirconium, Nat. Mater. 14 (9) (2015) 931–936.

[57] V. Bulatov, W. Cai, Computer Simulations of Dislocations, vol. 3, OUP Oxford, 2006.

[58] M. Tschopp, D. McDowell, Structures and energies of Σ 3 asymmetric tilt grain boundaries in copper and aluminium, Phil. Mag. 87 (22) (2007) 3147–3173.

[59] C. Barrett, T. Massalski, Structure of Metals, Crystallographic Methods, Principles, and Data, third ed., rev, PergamonPress, New York, 1980, pp. 256–259.

[60] N. Ashcroft, N. Mermin, Solid State Physics, Holt, Rinehart and Winston, vol. 2005, New York, 1976, p. 403.

[61] G. Simmons, Single Crystal Elastic Constants and Caluculated Aggregate Properties, A Handbook, vol. 4, MIT Press, 1971.

[62] Y. Wang, L.-Q. Chen, Z.-K. Liu, S. Mathaudhu, First-principles calculations of twin-boundary and stacking-fault energies in magnesium, Scr. Mater. 62 (9) (2010) 646–649.

[63] G. Voronoi, Nouvelles applications des paramètres continus à la théorie des formes quadratiques. Deuxième mémoire. Recherches sur les parallélloèdres primitifs, Journal für die reine und angewandte Mathematik (Crelles Journal) 1908 (134) (1908) 198–287.

[64] F. Aurenhammer, Voronoi diagrams—A survey of a fundamental geometric data structure, ACM Comput. Surv. 23 (3) (1991) 345–405.

[65] L. Huber, J. Rottler, M. Militzer, Atomistic simulations of the interaction of alloying elements with grain boundaries in Mg, Acta Mater. 80 (2014) 194–204.

[66] Z. Pei, R. Li, J.-F. Nie, J.R. Morris, First-principles study of the solute segregation in twin boundaries in Mg and possible descriptors for mechanical properties, Mater. Des. 165 (2019) 107574.

[67] Q. Yu, L. Qi, R.K. Mishra, J. Li, A.M. Minor, Reducing deformation anisotropy to achieve ultrahigh strength and ductility in Mg at the nanoscale, Proc. Natl. Acad. Sci. 110 (33) (2013) 13289–13293.

[68] K.Y. Xie, Z. Alam, A. Caffee, K.J. Hemker, Pyramidal I slip in c-axis compressed Mg single crystals, Scr. Mater. 112 (2016) 75–78.

[69] S. Ando, H. Tonda, Non-basal slips in magnesium and magnesium-lithium alloy single crystals, Mater. Sci. Forum 350 (2000) 43–48.

[70] H. Tonda, S. Ando, Effect of temperature and shear direction on yield stress by $\{11\bar{2}2\}<\bar{1}\bar{1}23>$ slip in HCP metals, Metall. Mater. Trans. A 33 (3) (2002) 831–836.

[71] I. Shin, E.A. Carter, Simulations of dislocation mobility in magnesium from first principles, Int. J. Plast. 60 (2014) 58–70.

[72] Y. Wang, H. Ye, On the tilt grain boundaries in HCP Ti with [0001] orientation, Phil. Mag. A 75 (1) (1997) 261–272.

[73] C. He, Z. Li, H. Chen, N. Wilson, J.-F. Nie, Unusual solute segregation phenomenon in coherent twin boundaries, Nat. Commun. 12 (1) (2021) 722.

[74] P. Mathews, S. Zhang, C. Scheu, R. Janisch, J. Neugebauer, T. Hickel, Solute induced defect phase transformations in Mg grain boundaries, 2023, arXiv preprint arXiv:2303.09585.

[75] D. McLean, A. Maradudin, Grain Boundaries in Metals, American Institute of Physics, 1958.

[76] C. White, W. Coghlan, Spectrum of binding energies approach to grain boundary segregation, Metall. Trans., A;(United States) 8 (9) (1977).

[77] M. Wagih, C.A. Schuh, Can symmetric tilt grain boundaries represent polycrystals? Scr. Mater. (2023) 115716.